Journal of Hazardous Materials 386 (2020) 121962

Contents lists available at ScienceDirect

Journal of Hazardous Materials

journal homepage: www.elsevier.com/locate/jhazmat

Revealing adsorption and the photodegradation mechanism of gas phase *o*-xylene on carbon quantum dots modified TiO_2 nanoparticles

Asad Mahmood*, Xiao Wang, Gansheng Shi, Zhuang Wang, Xiaofeng Xie, Jing Sun*

Shanghai Institute of Ceramics Chinese Academy of Sciences, 1295 Dingxi Road, Shanghai 200050, China

GRAPHICAL ABSTRACT

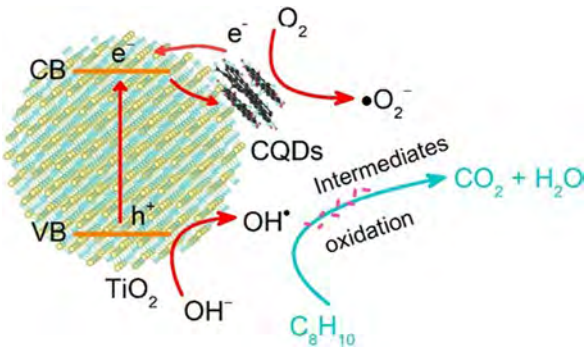

ARTICLE INFO

Editor: Danmeng Shuai

Keywords:
O-xylene
In-situ DRIFTS
Carbon quantum dots
TiO_2
DFT

ABSTRACT

Here, we report the photocatalytic oxidation (PCO) of *o*-xylene on carbon quantum dots (CQDs) modified TiO_2 nanoparticles. The results demonstrated that with 1 wt% CQDs loading, 87 % of *o*-xylene (50 ppm) can be photodegraded, which is 55.3 % higher than pure TiO_2 (56 %) under UV/visible light. This improved photocatalytic activity is associated with the important role of CQDs on TiO_2 surface, which increased the *o*-xylene adsorption and facilitated the photogenerated hole-electron separation process. Also, the 1 wt%CQDs/TiO_2 nanocomposite showed photocatalytic activity in the visible region ($\lambda > 400$ nm) compared to pure TiO_2 (inactive). The DFT study revealed that *o*-xylene strongly adsorb on TiO_2 (001) surface than (101) through π electrons of the aromatic ring. The in situ DRIFTS study showed that free OH groups on the photocatalyst surface could act as effective Lewis sides for the *o*-xylene adsorption. The interaction of π electrons of the aromatic ring and isolated OH groups was also observed. The FTIR peaks for CO_2 increased in the case of CQDs/TiO_2 nanocomposite contrasted to pure TiO_2, which suggested that the presence of CQDs improved the mineralization potency of TiO_2. These findings should affect the quest for a better photocatalyst to photodegrade VOCs.

1. Introduction

The major component of indoor air pollution is a low boiling point ($\leq$250 °C) volatile organic compounds (VOCs) (Liu et al., 2019; Fu et al., 2019). Amongst the typical VOCs, a substantial amount of xylene isomers (*ortho*, *meta*, *para*-xylene) are delivered to the atmosphere via natural and industrial operations (Yang et al., 2019; Sui et al., 2017). Xylene is used as a solvent and cleaning agent in different industrial sectors. The xylene derivatives might cause acute, i.e., eye-nose-throat (ENT), neurological, and chronic effects in humans, including

* Corresponding authors.
E-mail addresses: amkhan036@yahoo.com (A. Mahmood), jingsun@mail.sic.ac.cn (J. Sun).

https://doi.org/10.1016/j.jhazmat.2019.121962
Received 30 October 2019; Received in revised form 20 December 2019; Accepted 21 December 2019
Available online 23 December 2019
0304-3894/

headache, dizziness, kidney and coronary disease, exhaustion, and incoordination. Therefore, it is critical to manage and eliminate *o*-xylene in the indoor air environment. Consequently, efforts have been reported to control VOCs in the atmosphere, such as adsorption (Sun et al., 2014), catalytic combustion (Hu et al., 2018a), advanced oxidation (Liu et al., 2017), electrochemical (Lei et al., 2019), and photocatalytic methods (Dai et al., 2018). The application of these procedures is limited because of the large energy consumption and low efficiency for large scale implementation. On the other hand, the photocatalytic oxidation (PCO) of VOCs using metal oxides based semiconductor materials, for example, TiO_2, Co_3O_4, α-Fe_2O_3, CuO, Bi_2WO_6, CeO_2/$LaMnO_3$ provide opportunities to harness solar light, an inexpensive source of energy (Rao et al., 2019; Shi et al., 2018; Li et al., 2019).

Anatase TiO_2 (E_g = 3.2 eV) is a potential material for photocatalytic applications because of its stability, abundance, non-toxicity, and superior optical properties (Liu et al., 2018). However, the fast recombination of photogenerated hole-electron pairs limits the photocatalytic performance of TiO_2. Additionally, pure TiO_2 can only use light within the ultraviolet region (λ < 400 nm), which constitute 5 % of the solar spectrum, while 45 % of the solar spectrum is the visible region (Üzer et al., 2019). Along these lines, strategies have been adopted to promote the charge separation process, for example, impurity doping in TiO_2 crystal lattice (Umek et al., 2014), self-doping using Ti^{3+} (Zhang et al., 2014a), making composite frameworks along with other metal oxides and two-dimensional materials, including graphene and MoS_2 (Lu et al., 2013; He et al., 2019), and surface modification through metals (i.e., Pt, Rh, Au) deposition (Ohyama et al., 2011). The distinctive facets of TiO_2 NPs show significant variations in the atomic arraignments and surface energy, which affects the surface-catalyzed reactions (Li et al., 2015). For example, TiO_2 NPs preferentially grow along with low surface energy (0.43 J/m^2) (101) planes under normal growth conditions. However, the high energy (0.9 J/m^2) facets {001} are more reactive for the PCO process. TiO_2 {001} facets contain under-coordinated titanium and oxygen atoms such as the five-fold and two-fold coordinated Ti (Ti_{5c}) and oxygen atoms (O_{2c}), respectively. In contrast, the TiO_2 {101} facets exhibit 100 % six-fold coordinated Ti (Ti_{6c}) and three-fold oxygen (O_{3c}) atoms (Mahmood et al., 2019). The under-coordinated Ti_{5c} and O_{2c} play a significant role in the PCO process. Interestingly, these facets help in the separation of photoinduced hole-electron pairs (Kashiwaya et al., 2018). For example, the experimental evidence suggested that electrons predominantly transfer to the {101} facets, while holes migrate to the {001} facets. Based on these results, we can infer that (101) surface provides reducing sites while (001) surface provides oxidation sites. Therefore, because of the strong photooxidation potency of (001) surface, TiO_2 NPs with dominant {001} facets are much favored for the photocatalytic oxidation of VOCs.

Recently, zero-dimensional carbon quantum dots (CQDs) were used to sensitize TiO_2 for the antibacterial and photocatalytic applications (Liang et al., 2019). The CQDs have shown exceptional optical and electrical properties than its counterparts, such as graphene oxide and carbon nanotubes (CNTs). The CQDs are synthesized by simple synthesis routes, exhibiting excellent charge trapping potential and shape-dependent optical properties that make it useful for the photocatalysis (Laurenti et al., 2016). Unfortunately, the published literature is practically empty on the use of CQDs and TiO_2 composites in the photodegradation of gas-phase VOCs. Most of the scientific studies report only the photocatalytic activities in the liquid phase and applications in the energy direction (Liang et al., 2019; Li et al., 2017a). However, our group recently examined the photodegradation of acetaldehyde using CQDs/TiO_2 composites, and they accomplished some good results (Hu et al., 2018b). These results are encouraging to further investigate the potential of CQDs based TiO_2 nanocomposites for the photodegradation of gas-phase VOCs.

Considering the above, we report the photocatalytic degradation of *o*-xylene using CQDs decorated TiO_2 NPs with dominant {001} facets. Particularly, the CQDs/TiO_2 NPs showed high photocatalytic activity for the photodegradation of *o*-xylene in the UV/visible region than pure TiO_2. The CQDs/TiO_2 showed significant photocatalytic activity in the visible region, where pure TiO_2 was inactive. The in situ DRIFTS spectroscopy was further used to identify the intermediates in the photodegradation reaction. Also, we used the DFT study to grasp the adsorption mechanism of *o*-xylene on TiO_2 {001} and {101} facets. Similarly, we calculated the partial density of states (PDOS) and electron density difference (EDD) to differentiate the facet dependent behavior of TiO_2 NPs. These results are useful to develop a potential photocatalyst for the photodegradation of VOCs.

2. Materials and method

2.1. Synthesis of TiO_2

The starting materials, including titanium butoxide ($C_{16}H_{36}O_4Ti$; 97 %), sodium hydroxide (NaOH), 40 % aqueous solution of hydrogen fluoride (HF), and citric acid ($HOC(COOH)(CH_2COOH)_2$; ≥ 99.5 %) were received from Sigma-Aldrich. The solvents used are absolute ethanol and deionized water (ρ = 18.2 MΩ cm) purified through a Milli-Q Advantage A10 water purification system (Burlington, USA). A hydrothermal method was used to synthesize TiO_2 NPs with exposed {001} facets according to the previously reported method with little modifications (Shi et al., 2019). We employed strong acidic conditions to grow TiO_2 NPs with dominant {001} facets (Pan et al., 2011). Initially, 25 mL of $C_{16}H_{36}O_4Ti$ and 10 mL of HF were taken in a dry Teflon lying autoclave reactor. The reactor was firmly sealed and further enclosed in a steel reactor. The reactor was transferred to an electric furnace and kept at 200 °C for 24 h. Finally, the reactor was naturally cooled down to room temperature. The as-prepared powders were centrifuged and washed several times with deionized water. Next, the powders were dispersed in 0.1 M NaOH solution for 24 h to remove the surface fluoride ions. Finally, the powders were washed with deionized water and absolute ethanol and subsequently dried in an oven at 90 °C.

2.2. Synthesis of CQDs

CQDs were synthesized by the citrate decomposition method (Martindale et al., 2015). In a typical reaction, we treated 40 g of citric acid in a beaker at 180 °C for 40 h. An extended time frame is required to eliminate the undesirable residual organic matter. A dark orange-brown viscous mass (18 g) was achieved, which was cautiously dissolved in 5 M NaOH solution to reach the desired pH = 7. The as-prepared solution was freeze-dried to achieve CQDs powder and also to preserve the chemical structure.

2.3. Synthesis of CQDs of TiO_2 composites

The CQDs and TiO_2 composites were processed using the impregnation method. Typically, 1 g of TiO_2 NPs were dispersed in 20 mL (5 mL ethanol/15 mL water) solution of CQDs (0.01 g). The as-prepared solution was sonicated (2 h) and stirred (12 h) to produce a homogeneous mixture. Finally, the solution was slowly evaporated at 70 °C. The dried powder was further mill-mixed in a mortar and pestle. Finally, the mixture was calcined at different temperatures, for example, 100, 150, 200, and 300 °C. The sample calcined at 200 °C showed a high photocatalytic activity contrasted to other compositions; thus, we calcined the rest of the samples at 200 °C.

2.4. Characterization

The XRD study was used to identify the phase purity utilizing (Ultima IV 2036E102, Rigaku Corporation, Japan) X-ray diffractometer (Cu $K_{α1}$, (0.15406 nm)). The Perkin Elmer Lambda 950 UV/vis/NIR Spectrophotometer was used for the light absorption studies. A field-

emission scanning electron microscope (JEOL JSM-6700 F) was used to study particle morphology. HRTEM images were obtained using a high-resolution TEM JEOL 2100 with a LaB6 source operating at an acceleration voltage of 200 kV. Images were recorded on a Gatan Orius charge-coupled device. The powder was dropped-casted onto a 400 Cu mesh lacy carbon film grid (Agar Scientific Ltd.) for TEM analysis. The electron spin resonance signals (ESR) of the radicals were recorded using a model JES-FA200 spectrometer using 5,5-dimethyl-1-pyrroline N-oxide (DMPO) as a radical's trapper. The photoluminescence spectra analysis was carried out using an Edinburg FL/FS900 spectrometer with an excitation wavelength of 320 nm.

2.5. Adsorption capacity and photocatalytic activity

The photocatalytic degradation reaction of gaseous *o*-xylene was performed in an automated gas flow reactor (Fig. S1) operating at room temperature. The catalyst samples were prepared by milling the sample powder (0.1 g) in 10 mL ethanol for 20 min. The as-prepared slurry was coated on a glass substrate (16 × 13 cm) and eventually dried in an oven (80 °C for 2 h). The sample films were further transferred to the reaction chamber. At first, the *o*-xylene (50 ppm) was flown through the chamber in the dark at a constant flow rate (20 sccm) to achieve the adsorption-desorption equilibrium. The adsorption efficiency (E) of the sample gases, as well as the blank chamber, was calculated using Eqs. (1) and (2).

$$E_{catalyst} = \left\{ \left[\int_0^t v \times (1 - C/C_0) dt \right]_{catalyst} / \left[\int_0^t v \times (1 - C/C_0) dt \right]_{blank} \right\} \times 100\% \quad (1)$$

$$\left(E_{blank} = \left\{ \left[\int_0^{\sim t} v \times (1 - C/C_0) dt \right]_{blank} / \left[\int_0^t v \times (1 - C/C_0) dt \right]_{blank} \right\} \times 100\% = 100\% \right) \quad (2)$$

Where C_0 and C are initial gas concentration, different time interval flow rate is v, and t is the time interval of reaction. When the adsorption-desorption equilibrium was achieved, the samples were irradiated using a 400 W xenon lamp with an illumination density of 80 mW/cm^2 measured with THORLABS GmbH (PM100D; S314C detector) as the radiation source. We studied the photodegradation efficiency of TiO_2 NPs for acetaldehyde was studied with different flow rates under continuous irradiation. Based on these experiments, the conversion efficiency (φ) was calculated as $\varphi = (C_0 - C)/C_0 \times 100$ %.

2.6. In-situ DRIFTS

The in situ DRIFTS experiments were performed on an FTIR spectrometer (FT-IR, Bruker V70) equipped with a Praying Mantis diffuse reflection accessory from Harrick and an MCT detector. The catalyst in the DRIFT IR cell was pre-treated in 20 ml/min argon at 300 °C for 1 h. Subsequently, the background spectrum was recorded and subtracted from the sample spectrum obtained in the same condition. For the adsorption of *o*-xylene, the catalysts were exposed to the sample gas containing compressed air, 50 ppm of *o*-xylene, to get the time-dependent changes of the DRIFT spectra. A xenon light with an intensity of 500 W was used during the photodegradation of *o*-xylene.

2.7. Computational details

The adsorption energy, PDOS, and EDD were calculated using DFT calculations. All the calculations were performed using the Vienna Ab-initio Simulation Package (VASP) (Kresse and Hafner, 1993; av and Furthmuller, 1996; Kresse and Furthmuller, 1996). The bulk crystal lattice of TiO_2 was relaxed in a 2 × 2 × 2 supercell with a cutoff energy of 400 eV for the plane-wave expansion. The exchange and correlation energy were calculated using generalized gradient approximation (GGA) provided by Perdew-Burke-Erzhenhof (PBE) (Perdew et al., 1996). We additionally used the vdW-D correction method such as the pairwise force field given by Grimme to take into account the van der Waals forces (Grimme, 2006). The geometrically optimized bulk lattice was further used to model the desired facets of TiO_2 including {101} and {001}. The surface model contains 92 atoms and a vacuum of 20 Å was used to avoid interaction between the self-mirror images in calculations. The surface electronic configurations of the atoms are; Ti: [Ne] $3s^2 3p^6$; and O: [He] $2s^2 2p^6$. Only the top three layers and *o*-xylene molecules were allowed to relax during the calculations. The high adsorption energy models were further used for the PDOS and EDD calculations. The adsorption energy (E_{ads}) was calculated using Eq. (3).

$$\Delta E_{ads} = (E_{Molecule} + E_{Surface}) - E_{Molecule/Surface} \quad (3)$$

where $E_{Molecule}$ is the energy of a molecule in the gas phase, $E_{Surface}$ is the slab energy without adsorption and $E_{Molecule/Surface}$ is the energy of the surface and molecule complex.

3. Results and discussion

3.1. Phase, microstructure, optical, and SSA analysis

Fig. 1a shows the XRD peak profiles of the pure and CQDs/TiO_2 NPs. The major peaks identified at 2θ = 25.32°, 37.78°, 47.95°, 53.99°, 55.03°, and 62.72° conforming lattice planes (101), (004), (200), (105), (211), (206), and (116), respectively (*JCPDS card no: 21-1272*). The absence of impurity peaks confirmed the development of single phase anatase TiO_2 NPs. The corresponding cell parameters of the pure TiO_2 were calculated as $a = b = 3.7987$ Å and $c = 9.5214$ Å. A small variation in the lattice parameters of CQDs decorated TiO_2 is observed, which were calculated as $a = b = 3.7904$ Å and $c = 9.5325$ Å. These values are in close agreement with the previously reported values for anatase TiO_2 (Shin et al., 2019). The slightest change in the lattice parameter ($a = b = 0.23$ %; $c = 0.12$ %) with CQDs loading can be associated with additional temperature treatment (200 °C) in the course of CQDs impregnation. The particle morphology and elemental composition were examined using FESEM coupled with EDS. TiO_2 NPs with a truncated square-bipyramidal morphology can be viewed (Fig. 1b), displaying a characteristic growth behavior of anatase TiO_2 NPs with dominant {001} facets. The average particle size of TiO_2 NPs was measured as 68.2 nm using particle size distribution method (Fig. S2). The FESEM indicated a dissimilar particle size with well-defined morphology showing a somewhat similar shape. The related elemental mapping and composition confirmed Ti, O, and C as the main constituents (inset Table in Fig. 1).

Fig. 2a shows the TEM image of pure CQDs. The CQDs exhibited a spherical morphology. The mean particle diameter was measured as 2.4 nm (Fig. 2b). Fig. 2c and d show the TEM and HRTEM images of the CQDs/TiO_2 NPs. The HRTEM additionally validated the FESEM results in which the TiO_2 NPs seemed to exhibit truncated square-bipyramidal morphology. The top surface of the particles is regarded as {001} facet while the sides of the disks correspond to {101} facets. The lattice distance for CQDs was measured as 2.4 Å. The lattice distance 0.24 nm and 0.35 nm were attributed to anatase (001) and (101) TiO_2 planes, respectively. Interestingly, the TiO_2 particles revealed sharp edges, which describe the crystal growth of NPs in strong acidic condition and not the accumulation of small nanosheets. The HRTEM results confirmed the formation of desired pure and CQDs decorated TiO_2 NPs.

The light absorption properties of the pure and CQDs/TiO_2 NPs are shown in Fig. 3. The pure TiO_2 NPs demonstrated an absorption edge around 400 nm, which has been observed shifted to a high-frequency region for the CQDs/TiO_2 NPs indicating a redshift (Fig. 3a). These results proposed that the absorption of light can be substantially enhanced by CQDs impregnation on TiO_2. To further analyze charge transfer and recombination of hole-electron pairs in these samples, PL

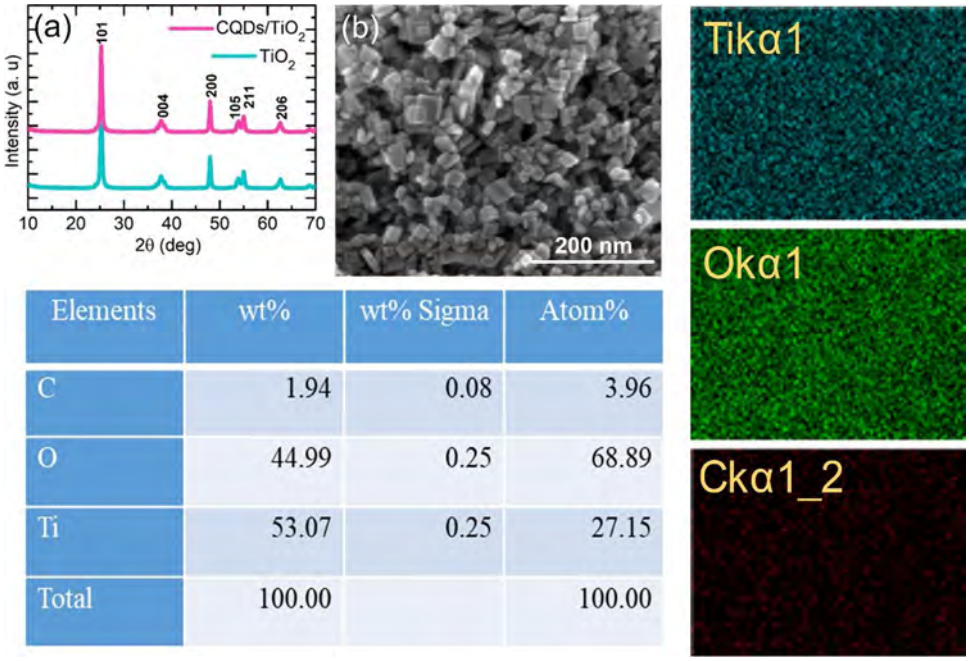

Elements	wt%	wt% Sigma	Atom%
C	1.94	0.08	3.96
O	44.99	0.25	68.89
Ti	53.07	0.25	27.15
Total	100.00		100.00

Fig. 1. XRD and microstructure analysis of CQDs decorated TiO_2 NPs, (a) XRD analysis, (b) FESEM image of TiO_2 NPs with elemental mapping. The inset Table shows elemental composition.

studies were carried out at room temperature using an excitation wavelength of 320 nm (Fig. 3b). The sample demonstrated a broad luminescence peak in the range extending from 350 to 550 nm, which centered around 400 nm. The center peak is caused by the band-band photoluminescence phenomena, which is related to the light energy comparable to the bandgap energy of TiO_2 (Abdulrazzak et al., 2016). Furthermore, the intensity of this centered peak significantly decreased for CQDs/TiO_2, indicating an effective charge separation process in CQDs/TiO_2 composite than pure TiO_2. This behavior can be described as follows; ideally, the light absorption in the UV/visible region triggers the transfer of electrons from the VB to CB. There are quite a few prospects for these energized electrons and holes, which includes recombination and trapping in impurity states (Chen et al., 2015). For the most part, the energized electrons are not consumed and recombine

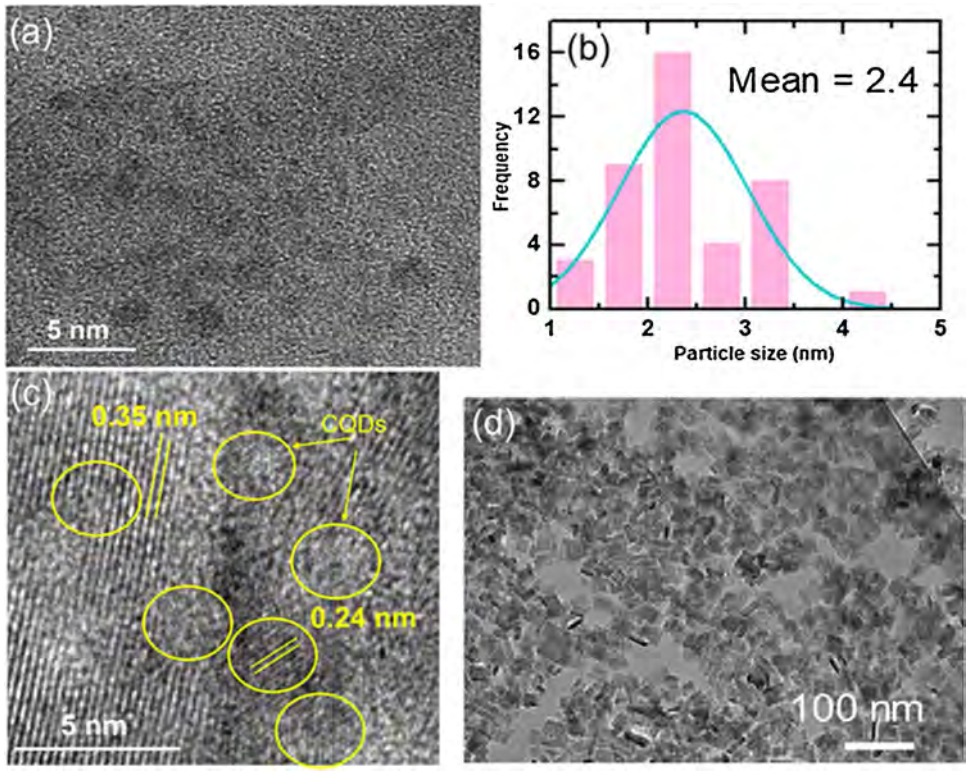

Fig. 2. (a) Typical TEM of pure CQDs, (b) particle size distribution histogram for pure CQDs, (c) TEM image of CQDs/TiO_2 NPs, (d) corresponding HRTEM image of CQDs/TiO_2 NPs.

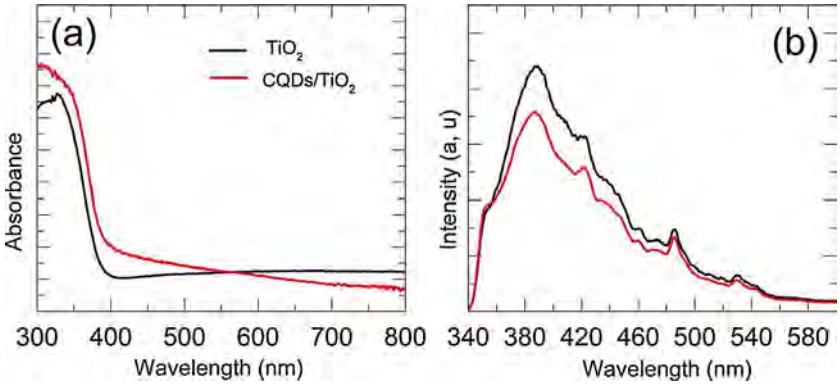

Fig. 3. Optical properties of TiO_2 and CQDs/TiO_2 nanocomposites, (a) UV/visible spectroscopy analysis, (b) PL spectra.

with the positive holes in a short span (nanoseconds). When the CQDs are available at the surface, the excited electrons further shuttle through the CQDs structural framework and therefore promote the charge separation process. Hence, it can be inferred that CQDs on TiO_2 surface significantly promoted the charge separation process.

The specific surface area (SSA) and the average pore diameter was calculated using nitrogen adsorption-desorption isotherm given in Fig. 4. The results suggested no significant difference in the specific SSA values. The SSA for the pure and CQDs decorated TiO_2 was calculated as 89 and 87 $m^2\,g^{-1}$, respectively. Similarly, the average pore diameter for the pure and CQDs modified TiO_2 was recorded as 2.049 and 1.600 nm, respectively.

3.2. Dynamic adsorption-desorption and photodegradation

The photodegradation of *o*-xylene was studied under UV/visible light illumination to analyze the photocatalytic performance of pure and CQDs/TiO_2 NPs (Fig. 5). Fig. 5a and c show the adsorption and photocatalytic degradation of *o*-xylene on CQDs/TiO_2 NPs calcined at different temperatures, respectively. The variation in calcination temperature during the CQDs impregnation process did affect the adsorption properties (Fig. 5a). The adsorption peak area was recorded as high for the composite calcined at 100 °C in contrast to pure TiO_2. A further rise in the calcination temperature improved the adsorption properties of the composite structures. For instance, the samples calcined at 200 and 300 °C exhibited 49 % and 88 % increase of *o*-xylene adsorption when compared with the blank chamber. The percent increase in the adsorption of CQDs/TiO_2 samples calcined at different temperatures is also given in Fig. 5b. The photodegradation curves under UV/visible illumination is provided in Fig. 5c. No considerable photocatalytic activity is recorded in the blank chamber (no catalyst). On the other hand, TiO_2 NPs showed an increase in the photodegradation efficiency, which has been recorded as 56 % (Fig. 5d). Moreover, the photodegradation of *o*-xylene was significantly enhanced by CQDs decoration on TiO_2. For example, the samples calcined at 200 °C revealed a higher photocatalytic response, exhibiting an efficiency of 87 %. With increasing calcination temperature, the photodegradation efficiency decreases to 61 % for the sample calcined at 300 °C. The results proposed that 200 °C is the optimum calcination temperature for producing the CQDs/TiO_2 composites by impregnation process showing excellent adsorption and photocatalytic activity for the gas phase *o*-xylene photodegradation.

The electron spin resonance (ESR) spectroscopy was further used to study the production ability of $^{\cdot}O_2^-$ and $^{\cdot}OH$ radicals (Fig. 6). The ESR spin trap technique was used to study the production of hydroxyl and oxygen species in the presence of pure and CQDs/TiO_2 NPs. The characteristic signals for the pure and CQDs decorated TiO_2 samples demonstrate the DMPO-O_2-and DMPO-OH adducts. The composite samples exhibited sharp signals for $^{\cdot}OH$ species than pure TiO_2. Likewise, pure TiO_2 showed high $^{\cdot}O_2^-$ signals compared with the CQDs/TiO_2 sample. The transfer of photoinduced electrons are facilitated due to high conductivity of CQDs, which might trap in the defects of CQDs sheets. Meanwhile, the hole mobility is prolonged which could produce high percentage of $^{\cdot}OH$ radicals in contrast to $^{\cdot}O_2^-$ radicals. In contrast, pure TiO_2 produces more mobile electrons, and consequently, more $^{\cdot}O_2^-$ radicals are created. Due to the high $^{\cdot}OH$ radical's production, better charge separation, and better light absorbing properties, the CQDs/TiO_2 NPs demonstrated a superior photocatalytic activity than pure TiO_2. Additionally, we studied the photodegradation of *o*-xylene on pure, and CQDs decorated TiO_2 NPs in the visible region, using a UV filter (> 400 nm) (Fig. S3). Interestingly, pure TiO_2 NPs did not show activity in the visible region; however, the CQDs decorated TiO_2 demonstrated a significant photodegradation efficiency (23 %) in the visible region. These results further prove that CQDs significantly improve the light harvesting efficiency of pure TiO_2, which is evidenced by the PL and high photodegradation of *o*-xylene in the UV/visible region. Hence, it can be inferred that CQDs sensitized TiO_2 due to wide visible absorption capability, which is evident from the optical characterization.

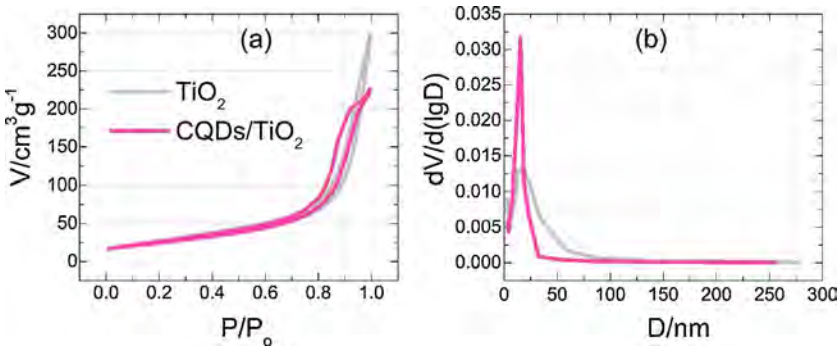

Fig. 4. (a) Nitrogen adsorption–desorption isotherm and (b) corresponding pore size distribution curves of pure and CQDs impregnated TiO_2.

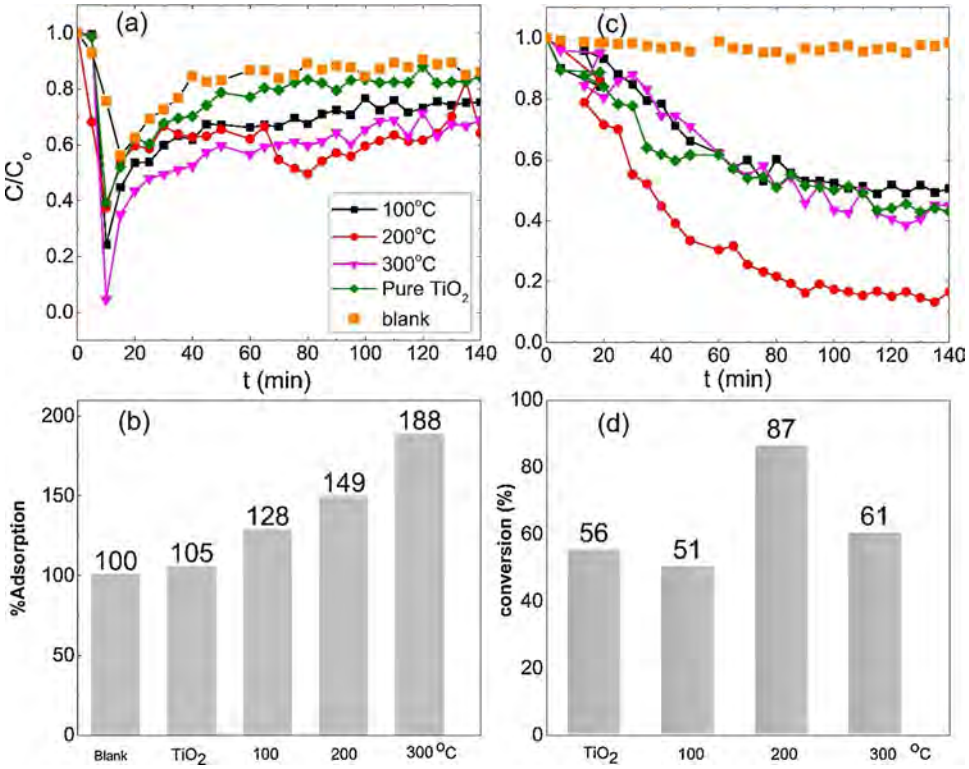

Fig. 5. (a) Adsorption and (c) photodegradation of *o*-xylene in the presence and absence of catalysts. The corresponding (b) percent adsorption, (d) conversion efficiency of *o*-xylene on pure and CQDs decorated TiO_2 NPs.

3.3. Computational analysis

We further studied the adsorption mechanism of *o*-xylene on pure TiO_2 using DFT calculations. Because of the structural intricacy of CQDs, only pure TiO_2 surface models are chosen to comprehend the adsorption mechanism of *o*-xylene. Since TiO_2 NPs exhibit two dominant facets including {101} and {001} in the XRD and HRTEM results, therefore, each facet was set up as a model in the DFT calculations. Before *o*-xylene adsorption, the desired surfaces of TiO_2 were relaxed (Fig. S4). The TiO_2 facets cleaved along (101) and (001) planes expose unique atomic arrangement on the surface. It is reported that TiO_2 {001} facet is photocatalytically more active due to the presence of undercoordinated five-folded Ti atoms (T_{5c}) and two-fold oxygen atoms (O_{2c}) on the surface (Sun and Zhang, 2016). On the other hand, the surface Ti (Ti_{6c}) and O (O_{3c}) atoms of TiO_2 {101} facet is fully coordinated, which deteriorate its reactivity. The top Ti—O bond length was measured as 1.827 Å while oxygen atom bonded to a bit lower titanium atom displayed an increasing bond distance of 1.864 Å in TiO_2 {101}. In the case of TiO_2 {001}, the Ti—O bond length was calculated as 1.951 Å. The geometrically optimized *o*-xylene molecule is shown in Fig. S4 with corresponding bond lengths. We analyzed the adsorption of *o*-xylene on TiO_2 (101) surface using different adsorption configurations (Fig. S5). The *o*-xylene molecule can interact with TiO_2 surface through the aromatic ring, hydrogen atoms of the ring, and the methyl groups. The calculated adsorption energies are given in Table 1. The low E_{ads} for various adsorption complexes, including T101A, T101B, T101C, and T101D suggested a poor interaction. Among the various configurations of *o*-xylene on TiO_2 (101), a high adsorption value was calculated for T101D, in which the aromatic ring oriented parallel on the surface and positioned above the surface oxygen. As a consequence of small E_{ads} values, it can be inferred that *o*-xylene only weakly binds on TiO_2 (101) surface. The related bond lengths in between different atoms are also given. For example, the length between *o*-xylene and surface was recorded as 3.11 Å (T101A). The shortest distance between the surface oxygen and hydrogen of the methyl group was recorded as 2.713 Å. Because of this weak interaction, no considerable distortion on the surface or in the molecule is visible. The Ti—O—Ti bond distance (1.832 Å) was observed to increase by 27 % when compared with this bond length (1.827 Å) in the pure surface. The results suggested that *o*-xylene interact with the top oxygen atom using aromatic π electrons of

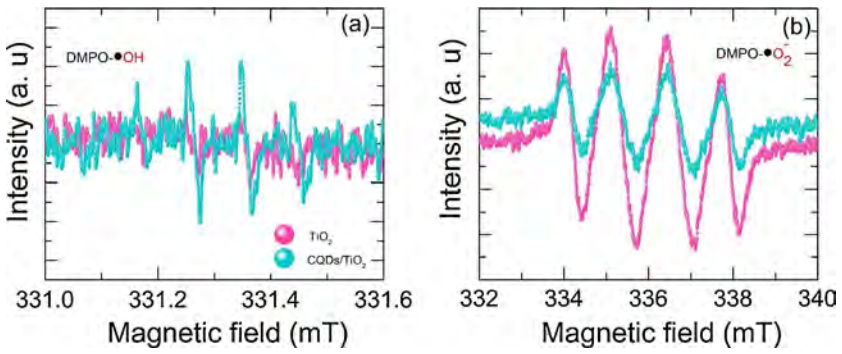

Fig. 6. ESR spectra of pure and CQDs decorated TiO_2 NPs under UV light irradiation.

Table 1
Calculated E_{ads} values for different configurations of *o*-xylene on TiO_2 {101} and {001} facets.

Conf.	E_{ads} (eV)			
	A	B	C	D
T101	0.219	0.129	0.131	0.239
T001	0.554	0.326	0.338	0.455

the ring. The high E_{ads} value recommended T101D as being the most stable adsorption configuration of *o*-xylene on TiO_2 (101) surface. The adsorption mechanism of *o*-xylene on TiO_2 (001) surface followed an identical configuration pattern (Fig. S6). The E_{ads} values suggested that *o*-xylene strongly adsorbed on TiO_2 (001) surface compared to TiO_2 (101) (Table 1). Much like TiO_2 (101), the adsorption complex (T001A) in which *o*-xylene molecule is parallel to the surface right above the surface oxygen (O_{2c}) gave a high adsorption energy value (E_{ads} = 0.554 eV). Furthermore, a significant distortion was observed on the surface. For example, the Ti_{5c}—O_{2c} bond length (2.158 Å) was observed to increase by 10 % when compared with the clean surface (1.951 Å). The aromatic ring distance from the surface O_{2c} was measured as 2.960 Å, that is quite shorter compared to a similar distance in T101D (3.010 Å). Also, the shortest distance between the aromatic ring hydrogen and surface O_{2c} (H—O_{2c}) was measured as 2.530 Å. Consequently, it can be inferred that *o*-xylene strongly adsorbed on TiO_2 (001) facet while only weakly interact with TiO_2 (101) facet. The E_{ads} values for other configurations, including T001B, T001C, and T001D suggested relatively weak interaction, but still stronger than TiO_2 (101). However, according to the calculated high adsorption energy value (0.554 eV), T001A is by far the most stable configuration of the *o*-xylene on TiO_2 (001).

Only, the most stable adsorption complexes were used for the PDOS and EDD calculations. The PDOS of the pure surface and *o*-xylene in the gas phase is given in Fig. S7. The PDOS of TiO_2 (101) and TiO_2 (001) surfaces demonstrated a significant variation in the available energy states; however, the contributions from different atoms were somewhat similar. In either case, $Ti_{(3p)}$ states weakly contributed in the upper CB (beyond 6 eV). In case of Ti (101), $Ti_{(3d)}$ states contributed in the CB around (1.82–7.20 eV) (Fig. S7a). However, this state occurred at relatively high energy started at 2.31–7.63 eV in Ti (001) (Fig. S7b). Additionally, $Ti_{(3d)}$ states also contributed to the VB around −4.78 to −0.74 eV. Interestingly, the $O_{(2p)}$ states, mainly contributed in the VB, where the energy states were well below the Fermi level (−4.90 to −0.36 eV) for TiO_2 (101). However, in the case of Ti (001), these states merged in the Fermi level (−3.78 to 0.32 eV). The PDOS of *o*-xylene (Fig. S7c) demonstrated characteristic sharp peaks. The respective contribution from different atoms is also given for comparison. The PDOS of the most stable complex's T101D and T001A is given in Fig. 7a and b, respectively. Some variations in the PDOS were observed, which can be traced by careful analysis. The intensity and position of the energy state's changed after the *o*-xylene adsorption. In T101D, the $Ti_{(3d)}$ states shifted to low energy (1.24 eV), and similarly, the intensity of the peak decreased. This states shifted to 2.06 eV compared to pure T001A (2.31 eV). Moreover, the intensity of peak significantly decreased contrasted to pure surface. The decrease in intensity of the energy states can be inferred as the occupation of free energy states, hence suggested coupling of different energy states. The intensity of the Cp energy states of the aromatic ring (rCp) at 4.8 eV decreased in T101D and T001A. The states around the Fermi level due to the *o*-xylene molecules behaves quite interestingly in both surfaces. For example, no significant shift was observed in the case of T101D; however, this peak significantly shifted to low energy values (in VB) in the case of T001A, demonstrating the stabilization of the adsorbate by adsorption of *o*-xylene on TiO_2 (001) surface. The $O_{(2p)}$ states and carbon p states of the aromatic ring (rCp) are strongly coupled near the Fermi level around −0.44 eV in T001A. The EDD for T101D and T001D is given in Fig. 7c and d, respectively. The green region represents the electron-rich region, while the purple region represents the electron depleting region. It is clear that the electron density surrounds the aromatic ring region and O_{2c}, thus confirming the π-electrons interaction of the aromatic ring. Additionally, this interaction also decreased the electron density surrounding the hydrogen atoms and converge more around the aromatic ring. This behavior is pronounced in the T001A compared to T101D. Moreover, a high charge density can be seen for T001A than T101D at the same isovalue (0.005) corresponding to high adsorption energy values. The EDD further confirmed the adsorption and PDOS results. The computational study suggested that TiO_2 NPs with dominant {001} facets are potentially more reactive to *o*-xylene adsorption.

3.4. In-situ DRIFTS analysis

The in-situ DRIFTS spectroscopy was used to further examine the adsorption and photodegradation of *o*-xylene on pure and CQDs/TiO_2 NPs. Initially, the samples were flushed with N_2 and the background spectrum was deduced. A series of adsorption spectra was recorded in the flow (flow rate of 20 sccm) of the reactant mixture (Fig. 8). The observed adsorption peaks are listed in Table S1. The broad peak around 3537 cm^{-1} is assigned to O—H stretching vibrations of the molecular water, that has been observed in both cases (Guo et al., 2019). The small peaks beyond 3537 cm^{-1} are attributed to isolated OH groups coordinated to Ti^{4+} on the surface (Sun and Zhang, 2016). These free OH groups act as effective Lewis sides for the *o*-xylene adsorption, which can be seen disappearing under the constant flow of *o*-xylene. This behavior is due to the interaction of the aromatic ring and O—H groups on the surface. Instead, a new broad complex peak with ill-defined maxima appear at low frequency (3132 and 3214 cm^{-1}), which evidenced the interaction of π electrons of the aromatic ring and isolated OH groups (Zhang et al., 2014b; Zheng et al., 2006). Several other adsorption peaks were observed in the range from 2800 to 3750 cm^{-1}, which could be associated with aromatic ring C—H groups and symmetric/asymmetric vibrations of the methyl groups C—H (Marie et al., 2005). The peaks beyond 3000 cm^{-1} is associated with C—H group of unsaturated C, while the ones below 3000 cm^{-1} are associated with C—H group of the saturated C (Klug and Forsling, 1999). The progressive peak at 2863 cm^{-1} is due to the symmetric stretching vibration of the methyl group (Fig. 8b) (Jang and Mcdow, 1997). The weak hump around 1271 cm^{-1} is due to aromatic ring vibration (Kovalevskiy et al., 2019). Similarly, the peaks around 1485 and 1619 cm^{-1} are associated with in-plane skeletal vibrations of the aromatic ring. These peaks are observed to increase with increasing adsorption time, while the similar type of peaks for CQDs/TiO_2 display high intensities in contrast to pure TiO_2. This behavior suggested that CQDs significantly improve the adsorption of *o*-xylene. This peak can be seen progressively increasing with increasing adsorption time in the beginning, which reaches to a somewhat steady level. The peaks around 1027 and 1071 cm^{-1} are associated with C—O stretching vibrations of the alkoxide species (Li et al., 2017b). These peaks are more noticeable in the CQDs/TiO_2 samples, which can be associated with the presence of CQDs that adsorb various oxygen and acetate groups.

Next, the samples were irradiated using UV/visible light and the photodegradation was recorded (Fig. 9). Various peaks were observed in both samples, and position of the peaks is slightly different in pure TiO_2 and CQDs/TiO_2 (Table S2); however, here we will only highlight the peak position of pure TiO_2 given in Fig. 9a and b (otherwise mentioned) while the CQDs/TiO_2 peaks are given in Fig. 9c, d. Several peaks can be traced during the photodegradation experiment (Fig. 9a, b), which can be attributed to the parent compound, intermediate species, and the converted product such as CO_2 and water. The peaks around 2334 and 2361 cm^{-1} are due to adsorbed CO_2 those are observed to increase in intensity with increasing photodegradation time (Wu et al., 2017). This behavior can be associated with the complete

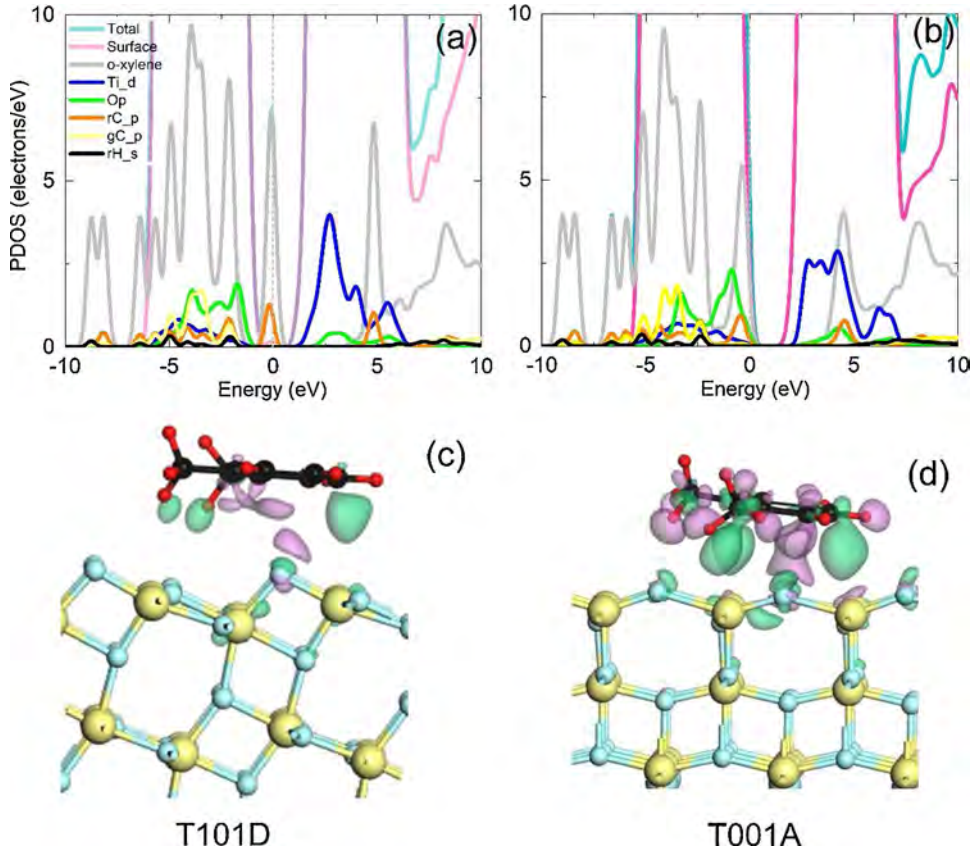

Fig. 7. PDOS of the most stable adsorption complexes, (a) Ti101A, (b) Ti001D. The corresponding EDD plots are given in (c) and (d), respectively.

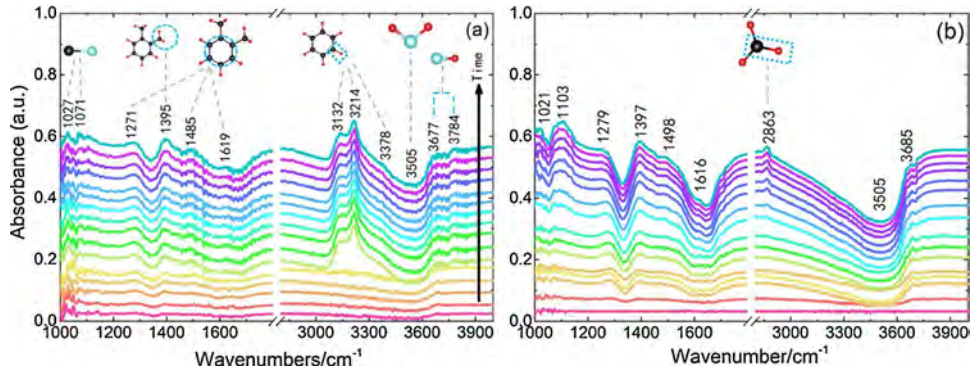

Fig. 8. FTIR spectra of *o*-xylene progressively adsorbed in the gas phase showing an increasing coverage with increasing time (step size 60 s) on (a) pure TiO_2, (b) CQDs/TiO_2.

oxidation of *o*-xylene on pure TiO_2. These peaks are sharpest in the case of CQDs/TiO_2 suggesting an increasing quantity of *o*-xylene mineralization compared to pure TiO_2. These results are in good agreement with our previous photodegradation experiment given in Fig. 5c and d, where CQDs/TiO_2 demonstrated a much higher photocatalytic activity than pure TiO_2. The small peaks at 3664, and 1641 cm^{-1} are attributed to bicarbonate vibrations. The peaks (i.e., 3727, 3791 cm^{-1}) beyond this range are associated with the depletion of isolated hydroxyl groups (Mino et al., 2016). The peaks are progressively stronger in CQDs/TiO_2 suggesting more hydroxyl groups are utilized in the composite structures compared to pure TiO_2. The broad peaks around the 3505 cm^{-1} are due to water associated OH groups. The peaks at 3214, 3141, and 3074 cm^{-1} are due to C—H group vibrations of the aromatic rings (Xie et al., 2017). Moreover, small peaks of aliphatic C—H group vibrations can be seen suggesting the formation of open chain compounds. New peaks in the range 1300 to 1850 cm^{-1} are arise in both samples, which are almost in the same position but with significant differences in shape. The sharp peaks in this range are due to various carbonyl groups of aldehydes and acids. Also, the intensity of these peaks increases with increasing photodegradation time, which can be attributed to the formation of the reaction intermediates, which covers the catalyst surface. These peaks can be identified based on the previously published literature (Li et al., 2019; Mino et al., 2016; Xie et al., 2017; Huang et al., 2008; Lai et al., 2019; Einaga et al., 2013). The small peak at 1776 cm^{-1} is associated with benzoic acid. The peaks at 1693 and 1720 cm^{-1} are due to C═O stretching vibrations. The peak at 1693, 1402, 1512 cm^{-1} are associated with *o*-toluadehyde. The peak at 1548 cm^{-1} is due to benzoate ion. The peak at 1564 and 1359 cm^{-1} is associated with COO– of carboxylate and format species. The peak at 1606 cm^{-1} is due to benzoquinone, while benzaldehyde give rise peaks at 1584 and 1199 cm^{-1}. The peaks below 1200 cm^{-1} are due to various C—O stretching vibrations adsorbed on the surface. The increasing

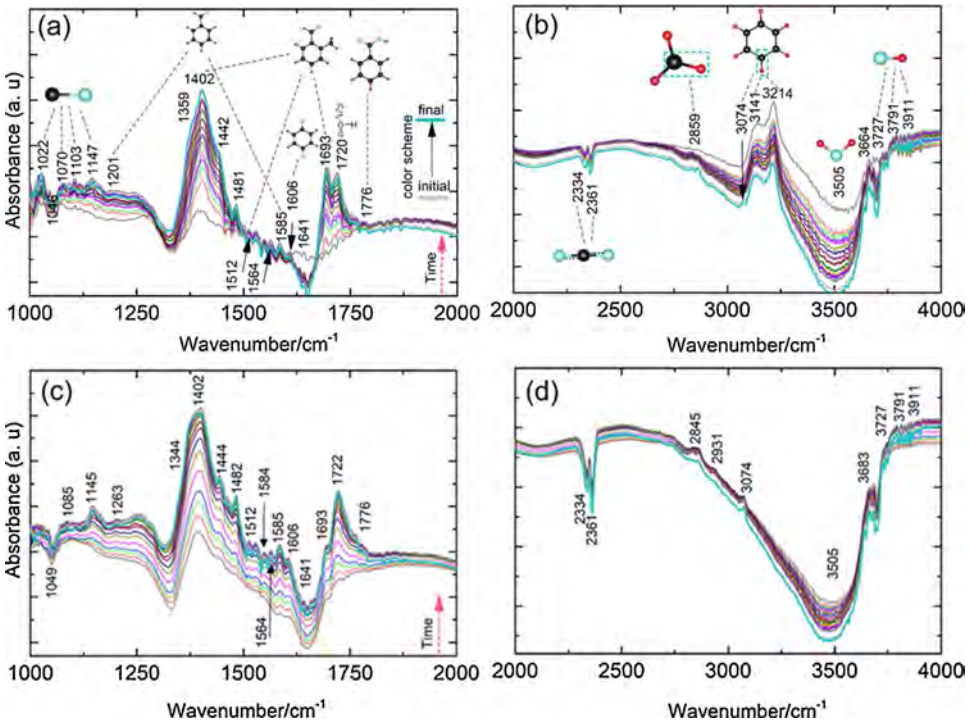

Fig. 9. FTIR spectra showing photodegradation of *o*-xylene with time (step size 60 s) under UV/visible illumination previously adsorbed on (a, b) pure TiO_2, (c, d) CQDs/TiO_2.

intensity also suggests the formation of more such groups as intermediates and product. The in-situ DRIFTS results suggested that the photodegradation of *o*-xylene involved various intermediate steps. Additionally, the results confirmed that a part of the *o*-xylene is completely mineralized while some part of the intermediates adsorb on the catalyst surface. Also, the in-situ DRIFTS results showed that CQDs significantly improved the photocatalytic performance of TiO_2 and a major part of the flowing gas is converted to the final product such as CO_2 and H_2O in contrast to pure TiO_2.

3.5. Proposed mechanism

Based on our experimental results, a proper proposed mechanism is given, which explains the adsorption and photodegradation of the flowing gas phase *o*-xylene on pure and CQDs modified TiO_2 NPs. The schematic view of photogenerated electrons and holes and subsequent photooxidation of *o*-xylene is shown in Fig. 10. The adsorption of the gas molecule is a crucial step for the gas phase photodegradation experiment. The experimental and computational results suggested that the adsorption capability of the pure TiO_2 NPs was significantly improved by CQDs. Although no significant difference in SSA was observed, CQDs modified TiO_2 improved the adsorption of *o*-xylene. This behavior can be associated with the available hexagonal ring structures in CQDs frameworks, which interact with the aromatic ring of *o*-xylene through π-π electrons. Additionally, due to the strong interaction of the CQDs with TiO_2 surface, the transport of photoexcited electrons becomes more efficient in the CQDs/TiO_2 composite structures, which is evidenced by the PL results. As stated earlier, TiO_2 {001} is composed of more under-coordinated Ti atoms on the surface, hence, more dioxygen species are adsorbed on the TiO_2 {001} facet, which further promote the charge transfer at the interface between the TiO_2 and adsorbed species and also obstruct the electron-hole recombination. The DFT results suggested that *o*-xylene strongly adsorbs on the TiO_2 (001) surface in contrast to (101) surface; therefore, in principle, TiO_2 NPs with dominant {001} facets must be more efficient for the *o*-xylene photodegradation reaction. When the CQDs are added, the light adsorption potency of the composite structure increased in contrast to pure TiO_2. As the in-situ DRIFTS analysis suggested that the photodegradation of the *o*-xylene is a very complex process that involves various intermediate species. However, the overall reaction mechanism can be described as follows. Initially, the ˙OH radicals attack the methyl groups of the *o*-xylene. Further reaction is driven by the ˙O_2– and ˙OH radicals, which can produce benzoquinone, benzaldehyde, formats and bicarbonate species, o-tolualdehyde, benzoic acid, and benzoate ions. Next, the ˙O_2– and ˙OH radicals further promote the reaction, and a chain of smaller intermediates are produced. Finally, the intermediates are converted into a product, such as CO_2 and H_2O. The ESR study suggested that CQDs/TiO_2 composite generates more ˙OH radicals and less ˙O_2– radicals in contrast to pure TiO_2. Therefore, the steps that involve the ˙OH radicals will be enhanced significantly by the addition of CQDs and vice versa. We further studied the recyclability of CQDs/TiO_2 photocatalyst (Fig. 11). No significant variations could be observed after five cycles demonstrating the stability and potency of our

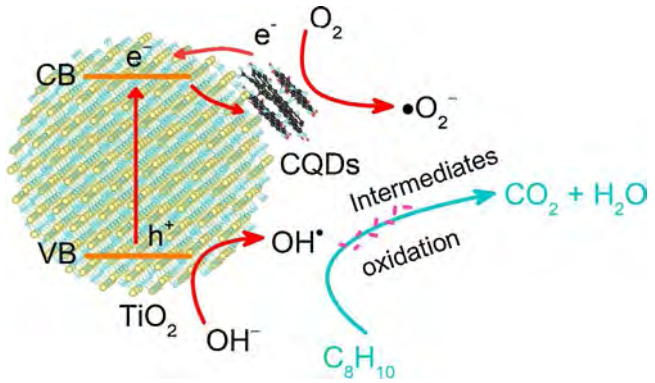

Fig. 10. A proposed mechanism depicting electronic excitation in TiO_2, intermediate formation, and the photocatalytic oxidation process of *o*-xylene on CQD_S/TiO_2. Nomenclature of molecular structures include, C: black, O: light blue, H: red.

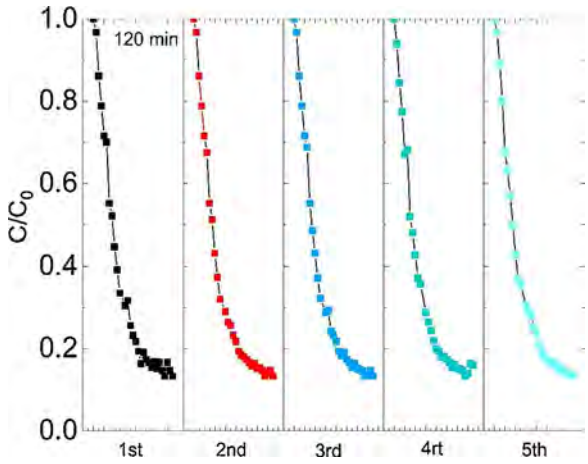

Fig. 11. Recycle run of the CQDs/TiO_2 for the photodegradation of *o*-xylene under UV/visible irradiation.

photocatalyst for the practical device frameworks.

4. Conclusion

In summary, CQDs decorated TiO_2 nanoparticles were successfully synthesized and studied their adsorption capability and photodegradation efficiency for the gas-phase *o*-xylene. The light absorption and charge separation were improved in TiO_2 NPs via CQDs decoration, which were confirmed by the UV/visible and PL studies. As pure TiO_2 showed no photocatalytic activity in the visible region, CQDs/TiO_2 nanocomposites demonstrated a considerable photodegradation efficiency (23 %). Moreover, the adsorption properties of TiO_2 was greatly improved by CQDs signifying its positive effect for the gas phase reactions. The DFT calculations further confirmed that *o*-xylene strongly attaches to TiO_2 (001) surface, while only weakly adsorbed on TiO_2 (101) surface. The in situ DRIFTS study suggested that the photocatalytic oxidation of *o*-xylene involved several intermediates formation. Briefly, it can be inferred that due to CQDs on TiO_2 surface, the π-π electron interaction between the aromatic ring of *o*-xylene and CQDs resulted in an increasing adsorption capability. Also, the CQDs increased the production of $^{\cdot}OH$ radicles that was confirmed through ESR study, which further enhanced the photocatalytic oxidation process. This study suggests that CQDs is a promising inexpensive source, which can be used as a co-catalyst for improving the photocatalytic properties of TiO_2 to develop an efficient and inexpensive photocatalyst for the commercial use.

CRediT authorship contribution statement

Asad Mahmood: Conceptualization, Methodology, Data curation, Investigation, Funding acquisition, Writing - original draft. **Xiao Wang:** Formal analysis, Funding acquisition. **Gansheng Shi:** Investigation, Methodology. **Zhuang Wang:** Data curation, Validation. **Xiaofeng Xie:** Supervision. **Jing Sun:** Supervision.

Declaration of Competing Interest

The authors declare that they have no known competing financial interests or personal relationships that could have appeared to influence the work reported in this paper.

Acknowledgments

The authors are thankful for the financial support under the CAS President's International Fellowship Initiative (PIFI) program (2018PE0014), National Key Research and Development Program of China (2016YFA0203000), NSFC-DFG bilateral organization program (51761135107), Shanghai Sailing Program (18YF1426800), and the Innovation Program of Shanghai Institute of Ceramics, Chinese Academy of Sciences.

Appendix A. Supplementary data

Supplementary material related to this article can be found, in the online version, at doi:https://doi.org/10.1016/j.jhazmat.2019.121962.

References

Abdulrazzak, F.H., Hussein, F.H., Alkaim, A.F., Ivanova, I., Emeline, A.V., Bahnemann, D.W., 2016. Sonochemical/hydration-dehydration synthesis of Pt-TiO_2 NPs/decorated carbon nanotubes with enhanced photocatalytic hydrogen production activity. Photochem. Photobiol. Sci. 15, 1347–1357.

av, G.K., Furthmuller, J., 1996. Efficiency of ab-initio total energy calculations for metals and semiconductors using a plane-wave basis set. Comput. Mater. Sci. 6, 15–50.

Chen, H., Tang, M., Rui, Z., Ji, H., 2015. MnO_2 promoted TiO_2 nanotube array supported Pt catalyst for formaldehyde oxidation with enhanced efficiency. Ind. Eng. Chem. Res. 54, 8900–8907.

Dai, C., Zhou, Y., Peng, H., Huang, S., Qin, P., Zhang, J., Yang, Y., Luo, L., Zhang, X., 2018. Current progress in remediation of chlorinated volatile organic compounds: a review. J. Ind. Eng. Chem. 62, 106–119.

Einaga, H., Mochiduki, K., Teraoka, Y., 2013. Photocatalytic oxidation processes for toluene oxidation over TiO_2 catalysts. Catalysts 3, 219–231.

Fu, S., Zheng, Y., Zhou, X., Ni, Z., Xia, S., 2019. Visible light promoted degradation of gaseous volatile organic compounds catalyzed by Au supported layered double hydroxides: influencing factors, kinetics and mechanism. J. Hazard. Mater. 363, 41–54.

Grimme, S., 2006. Semiempirical GGA-type density functional constructed with a long-range dispersion correction. J. Comput. Chem. 27, 1787–1799.

Guo, C., Guo, X., Chu, W., Jiang, N., Li, H., 2019. FTIR-ATR study for adsorption of trypsin in aqueous environment on bare and TiO_2 coated ZnSe surfaces. Chin. Chem. Lett.

He, X., Fang, H., Gosztola, D.J., Jiang, Z., Jena, P., Wang, W.N., 2019. Mechanistic insight into photocatalytic pathways of MIL-100(Fe)/TiO_2 composites. ACS Appl. Mater. Interfaces 11, 12516–12524.

Hu, J., Li, W.B., Liu, R.F., 2018a. Highly efficient copper-doped manganese oxide nanorod catalysts derived from CuMnO hierarchical nanowire for catalytic combustion of VOCs. Catal. Today 314, 147–153.

Hu, Y., Xie, X., Wang, X., Wang, Y., Zeng, Y., Pui, D.Y.H., Sun, J., 2018b. Visible-light upconversion carbon quantum dots decorated TiO_2 for the photodegradation of flowing gaseous acetaldehyde. Appl. Surf. Sci. 440, 266–274.

Huang, S., Zhang, C., He, H., 2008. Complete oxidation of o-xylene over Pd/Al_2O_3 catalyst at low temperature. Catal. Today 139, 15–23.

Jang, Myoseon, Mcdow, S.R., 1997. Products of benz[a]anthracene photodegradation in the presence of known organic constituents of atmospheric aerosols. Environ. Sci. Technol. 31, 1046–1053.

Kashiwaya, S., Toupance, T., Klein, A., Jaegermann, W., 2018. Fermi level positions and induced band bending at single crystalline anatase (101) and (001) surfaces: origin of the enhanced photocatalytic activity of facet engineered crystals. Adv. Energy Mater. 8 1802195 (1802191-1802197).

Klug, O., Forsling, W., 1999. A spectroscopic study of phthalate adsorption on γ-aluminum oxid. Langmuir 15, 6961–6968.

Kovalevskiy, N.S., Selishcheva, S.A., Solovyeva, M.I., Selishchev, D.S., 2019. In situ IR spectroscopy data and effect of the operational parameters on the photocatalytic activity of N-doped TiO_2. Data Brief 24, 103917.

Kresse, G., Furthmuller, J., 1996. Efficient iterative schemes for ab initio total-energy calculations using a plane-wave basis set. Phys. Rev. B 54, 169–186.

Kresse, G., Hafner, J., 1993. Ab initiomolecular dynamics for liquid metals. Phys. Rev. B 47, 558–561.

Lai, M., Zhao, J., Chen, Q., Feng, S., Bai, Y., Li, Y., Wang, C., 2019. Photocatalytic toluene degradation over Bi-decorated TiO_2: promoted O_2 supply to catalyst's surface by metallic Bi. Catal. Today 335, 372–380.

Laurenti, M., Paez-Perez, M., Algarra, M., Alonso-Cristobal, P., Lopez-Cabarcos, E., Mendez-Gonzalez, D., Rubio-Retama, J., 2016. Enhancement of the upconversion emission by visible-to-near-infrared fluorescent graphene quantum dots for miRNA detection. ACS Appl. Mater. Interfaces 8, 12644–12651.

Lei, C., Liang, F., Li, J., Chen, W., Huang, B., 2019. Electrochemical reductive dechlorination of chlorinated volatile organic compounds (Cl-VOCs): effects of molecular structure on the dehalogenation reactivity and mechanisms. Chem. Eng. J. 358, 1054–1064.

Li, C., Koenigsmann, C., Ding, W., Rudshteyn, B., Yang, K.R., Regan, K.P., Konezny, S.J., Batista, V.S., Brudvig, G.W., Schmuttenmaer, C.A., Kim, J.H., 2015. Facet-dependent photoelectrochemical performance of TiO_2 nanostructures: an experimental and computational study. J. Am. Chem. Soc. 137, 1520–1529.

Li, H., Shi, W., Huang, W., Yao, E.P., Han, J., Chen, Z., Liu, S., Shen, Y., Wang, M., Yang, Y., 2017a. Carbon quantum dots/TiOx electron transport layer boosts efficiency of planar heterojunction perovskite solar cells to 19. Nano Lett. 17, 2328–2335.

Li, K., Chen, J., Bai, B., Zhao, S., Hu, F., Li, J., 2017b. Bridging the reaction route of toluene total oxidation and the structure of ordered mesoporous Co_3O_4: the roles of surface sodium and adsorbed oxygen. Catal. Today 297, 173–181.

Li, J.-J., Yu, E.-Q., Cai, S.-C., Chen, X., Chen, J., Jia, H.-P., Xu, Y.-J., 2019. Noble metal free, $CeO_2/LaMnO_3$ hybrid achieving efficient photo-thermal catalytic decomposition of volatile organic compounds under IR light. Appl. Catal. B Environ. 240, 141–152.
Liang, Z., Hou, H., Fang, Z., Gao, F., Wang, L., Chen, D., Yang, W., 2019. Hydrogenated TiO_2 nanorod arrays decorated with carbon quantum dots toward efficient photoelectrochemical water splitting. ACS Appl. Mater. Interfaces 11, 19167–19175.
Liu, G., Ji, J., Huang, H., Xie, R., Feng, Q., Shu, Y., Zhan, Y., Fang, R., He, M., Liu, S., Ye, X., Leung, D.Y.C., 2017. UV/H_2O_2: an efficient aqueous advanced oxidation process for VOCs removal. Chem. Eng. J. 324, 44–50.
Liu, L., Pan, F., Liu, C., Huang, L., Li, W., Lu, X., 2018. TiO_2 nanofoam–nanotube array for surface-enhanced raman scattering. ACS Appl. Nano Mater. 1, 6563–6566.
Liu, C., Zhang, X., Wang, Q., Shi, K., 2019. Role of PM2.5 in the photodegradation of the atmospheric benzene. Environ. Pollut. 247, 447–456.
Lu, J., Deng, C., Zhang, X., Yang, P., 2013. Synthesis of Fe_3O_4/graphene/TiO_2 composites for the highly selective enrichment of phosphopeptides from biological samples. ACS Appl. Mater. Interfaces 5, 7330–7334.
Mahmood, A., Shi, G., Xie, X., Sun, J., 2019. Adsorption mechanism of typical oxygen, sulfur, and chlorine containing VOCs on TiO_2 (0 0 1) surface: first principle calculations. Appl. Surf. Sci. 471, 222–230.
Marie, O., Thibaultstarzyk, F., Massiani, P., 2005. Conversion of xylene over mordenites: an operando infrared spectroscopy study of the effect of Na+. J. Catal. 230, 28–37.
Martindale, B.C., Hutton, G.A., Caputo, C.A., Reisner, E., 2015. Solar hydrogen production using carbon quantum dots and a molecular nickel catalyst. J. Am. Chem. Soc. 137, 6018–6025.
Mino, L., Zecchina, A., Martra, G., Rossi, A.M., Spoto, G., 2016. A surface science approach to TiO_2 P25 photocatalysis: an in situ FTIR study of phenol photodegradation at controlled water coverages from sub-monolayer to multilayer. Appl. Catal. B: Environ. 196, 135–141.
Ohyama, J., Yamamoto, A., Teramura, K., Shishido, T., Tanaka, T., 2011. Modification of metal nanoparticles with TiO_2 and metal − support interaction in photodeposition. ACS Catal. 1, 187–192.
Pan, J., Liu, G., Lu, G.Q., Cheng, H.M., 2011. On the true photoreactivity order of {001}, {010}, and {101} facets of anatase TiO_2 crystals. Angew. Chem. Int. Ed. Engl. 50, 2133–2137.
Perdew, John P., Burke, Kieron, Ernzerhof, M., 1996. Generalized gradient approximation made simple. Phys. Rev. Lett. 77, 3865–3868.
Rao, Z., Xie, X., Wang, X., Mahmood, A., Tong, S., Ge, M., Sun, J., 2019. Defect chemistry of Er^{3+}-doped TiO_2 and its photocatalytic activity for the degradation of flowing gas-phase vocs. J. Phys. Chem. C 123, 12321–12334.
Shi, Z., Lan, L., Li, Y., Yang, Y., Zhang, Q., Wu, J., Zhang, G., Zhao, X., 2018. Co_3O_4/TiO_2 nanocomposite formation leads to improvement in ultraviolet–visible-infrared-driven thermocatalytic activity due to photoactivation and photocatalysis–thermocatalysis synergetic effect. ACS Sustain. Chem. Eng. 6, 16503–16514.
Shi, G., Mahmood, A., Lu, G., Wang, X., Tong, S., Ge, M., Xie, X., Sun, J., 2019. Adsorption and photodegradation of acetaldehyde and ethylene on TiO_2 (001) surface: experimental and first principle studies. Catal. Lett. 1–11.
Shin, W.J., Granados, A.H., Huang, W.-H., Hu, H., Tao, M., 2019. Sulfurization of hematite Fe_2O_3 and anatase TiO_2 by annealing in H_2S. Mater. Chem. Phys. 222, 152–158.
Sui, H., An, P., Li, X., Cong, S., He, L., 2017. Removal and recovery of o- xylene by silica gel using vacuum swing adsorption. Chem. Eng. J. 316, 232–242.
Sun, X., Miao, J., Xiao, J., Xia, Q., Zhao, Z., 2014. Heterogeneity of adsorption sites and adsorption kinetics of n-hexane on metal–organic framework MIL-101(Cr). Chin. J. Chem. Eng. 22, 962–967.
Sun, S., Zhang, F., 2016. Insights into the mechanism of photocatalytic degradation of volatile organic compounds on TiO_2 by using in-situ DRIFTS. Semiconductor Photocatalysis-Materials, Mechanisms and Applications. pp. Fermi level positions and induced band bending at single crystalline anatase (101) and (001) surfaces: origin of the enhanced photocatalytic activity of facet engineered crystals.
Umek, P., Bittencourt, C., Guttmann, P., Gloter, A., Škapin, S.D., Arčon, D., 2014. Mn2+ substitutional doping of TiO_2 nanoribbons: a three-step approach. J. Phys. Chem. C 118, 21250–21257.
Üzer, E., Kumar, P., Kisslinger, R., Kar, P., Thakur, U.K., Zeng, S., Shankar, K., Nilges, T., 2019. Vapor deposition of semiconducting phosphorus allotropes into TiO2 nanotube arrays for photoelectrocatalytic water splitting. Acs Appl. Nano Mater. 2, 3358–3367.
Wu, Y., Yuan, S., Feng, R., Ma, Z., Gao, Y., Xing, S., 2017. Comparative study for low-temperature catalytic oxidation of o-xylene over doped OMS-2 catalysts: role of Ag and Cu. Mol. Catal. 442, 164–172.
Xie, S., Liu, Y., Deng, J., Yang, J., Zhao, X., Han, Z., Zhang, K., Dai, H., 2017. Insights into the active sites of ordered mesoporous cobalt oxide catalysts for the total oxidation of o-xylene. J. Catal. 352, 282–292.
Yang, C., Miao, G., Pi, Y., Xia, Q., Wu, J., Li, Z., Xiao, J., 2019. Abatement of various types of VOCs by adsorption/catalytic oxidation: a review. Chem. Eng. J. 370, 1128–1153.
Zhang, Z., Yang, X., Hedhili, M.N., Ahmed, E., Shi, L., Wang, P., 2014a. Microwave-assisted self-doping of TiO_2 photonic crystals for efficient photoelectrochemical water splitting. ACS Appl. Mater. Interfaces 6, 691–696.
Zhang, F., Zhu, X., Ding, J., Qi, Z., Wang, M., Sun, S., Bao, J., Gao, C., 2014b. Mechanism study of photocatalytic degradation of gaseous toluene on TiO_2 with weak-bond adsorption analysis using in situ far infrared spectroscopy. Catal. Lett. 144, 995–1000.
Zheng, S., Jentys, A., Lercher, J., 2006. Xylene isomerization with surface-modified HZSM-5 zeolite catalysts: an in situ IR study. J. Catal. 241, 304–311.